Astronomy & Astrophysics manuscript no.
(will be inserted by hand later)

Multiple scattering of polarized radiation by non-spherical grains: first results

S. Wolf[1], N.V. Voshchinnikov[2], and Th. Henning[3]

[1] Thuringian State Observatory Tautenburg, Sternwarte 5, D-07778 Tautenburg, Germany
[2] Sobolev Astronomical Institute, St. Petersburg University, Bibliotechnaya pl. 2, 198504 St. Petersburg-Peterhof, Russia and Isaac Newton Institute of Chile, St. Petersburg Branch
[3] Astrophysical Institute and University Observatory, Friedrich Schiller University, Schillergäßchen 3, D-07745 Jena, Germany

Received <date> / Accepted <date>

Abstract. We present the first solution to the radiative transfer problem in dust configurations containing aligned non-spherical (spheroidal) dust grains. The optical properties of spheroidal grains are calculated using the method of separation of variables developed by Voshchinnikov & Farafonov (1993). The radiative transfer problem is solved on the basis of a Monte-Carlo method for three-dimensional self-consistent simulations (Wolf et al. 1999). The test simulations confirming the correct numerical implementation of the scattering mechanism are presented. As a first application, we investigate the linear and circular polarization from a spherical circumstellar shell containing perfectly aligned prolate or oblate spheroidal grains. The dependence of the results on the grain parameters (equivolume radius, aspect ratio) and the shell parameters (inner/outer radius, optical thickness) is considered. The most remarkable features of the simulated linear polarization maps are so-called polarization null points where the reversal of polarization occurs. They appear in the case when the grain alignment axis is perpendicular to the line of sight. The position of these points may be used for the estimation of grain shape and geometrical structure of the shell. The maps of circular polarization has the sector-like structure with maxima at the ends of line inclined to the grain alignment axis by $\pm 45°$.

Key words. Polarization – Radiative transfer – Scattering – Methods: numerical – (Stars:) circumstellar matter – ISM: clouds

1. Introduction

It is now well established that the polarization of optical radiation from young and evolved stellar objects, reflection nebulae, and active galactic nuclei is mainly caused by dust grains. In many cases the observed polarization can be satisfactorily interpreted in the frame of light scattering by spherical grains. In particular, the orientation of the polarization vectors is often used for the identification and location of the illuminating source inside the dust configuration or the investigation of its geometrical structure.

However, even in the case of rather simple objects like ordinary reflection nebulae, the deviations of polarization vectors from the direction perpendicular to a star were discovered many years ago (Elvius & Hall 1967). These deviations are displayed in the outer filamentary parts of the Merope nebula and are connected with the light scattering by non-spherical grains aligned by the magnetic field directed along the filaments. Non-centrosymmetric polarization patterns were observed in bipolar and cometary nebulae (Scarrott et al. 1989), young stellar objects (Hajjar & Bastien 1996), evolved stars (Kastner & Weintraub 1996), and are clearly seen in polarization maps of comets (Dollfus & Suchail 1987).

Another effect which may be related to the light scattering by non-spherical grains is the wavelength dependence of the positional angle of polarization observed in red giants, AGB stars, and protoplanetary nebulae (see, e.g., Johnson & Jones 1991). The variations from blue to red may reach $20° - 60°$ and it is very difficult or impossible to interpret them using the spherical grains only.

Recently, very high circular polarization of scattered light in the Orion molecular cloud was observed by Chrysostomou et al. (2000). The authors suggest that the circular polarization is produced by aligned grains.

In addition, the interstellar polarization and polarized thermal emission phenomena prove that non-spherical grains exist in the interstellar medium. These effects arise because of dichroic extinction/emission of radi-

Send offprint requests to: N.V. Voshchinnikov, e-mail: nvv@dust.astro.spbu.ru

ation by aligned non-spherical grains and were modeled with spheroidal grains (Voshchinnikov 1990; Kim & Martin 1995; Il'in & Henning 2000; Onaka 2000).

Up to now, spheroidal grains have been used for the interpretation of scattered radiation in the case of single scattering only (Voshchinnikov 1998; Gledhill & McCall 2000).

The solution to the problem of multiple scattering of polarized radiation by non-spherical particles is extremely difficult and even for spherical grains almost all considerations made are based on Monte Carlo simulation. This method was used for the interpretation of polarimetric observations of various stars (e.g., Daniel 1980; Voshchinnikov & Karjukin 1994) as well as the production of polarimetric maps of different extended objects (Bastien & Ménard 1988; Fischer et al. 1994; Wolf et al. 1998).

The most recent achievement of the Monte Carlo technique is the development of a multidimensional self-consistent radiative transfer (RT) code that allows to calculate the spectral energy distribution of various dust configurations (Wolf et al. 1999; Wolf & Henning 2000).

The main aim of this paper is to provide the first complete solution to the polarized radiation transfer problem including scattering, extinction, absorption, and re-emission of radiation by aligned spheroidal dust grains. We are going to apply the formalism developed to several simple model configurations.

Because of the complexity of the problem, we decided to consider the separate mechanisms step by step. In this paper we present the basic theory (Sect. 2), describe main numerical features (Sect. 3), and consider multiple scattering of light by spheroidal grains and the resulting linear and circular polarization (Sect. 4 and 5).

2. Basics

2.1. Radiative transfer with non-spherical particles

The main features distinguishing the light scattering by aligned non-spherical particles and spherical particles are:

- azimuthal dependence of the scattered radiation;
- non-zero linear polarization in the forward and backward directions;
- rotation of the positional angle of linear polarization after first scattering;
- non-zero circular polarization after first scattering.

These features result from the fact that in general case for non-spherical particles all 16 elements of the scattering matrix are non-zero.

We suppose that the grains are prolate or oblate homogeneous spheroids with an aspect ratio a/b (a and b are the major and minor semiaxes of a spheroid, respectively).

The particle size will be characterized by the radius $r_{\rm V}$ of the sphere whose volume is equal to that of a spheroid. The major semiaxis of the spheroid is connected with $r_{\rm V}$ as follows:

$$a = r_{\rm V}(a/b)^{2/3} \tag{1}$$

for prolate spheroids and

$$a = r_{\rm V}(a/b)^{1/3} \tag{2}$$

for oblate ones.

The optical properties of a particle also depend on the refractive index of the grain material m_λ and the angle α between the rotation axis of the spheroid and the wavevector ($0^\circ \le \alpha \le 90^\circ$).

The RT simulation includes the following processes depending on grain properties:

- simulation of the length of the photon free mean path using the optical distance in a given direction (Sect. 2.2.1);
- photon scattering described by the scattering matrix (Sect. 2.2.2);
- photon absorption described by the particle albedo (Sect. 2.2.3);
- photon re-emission described by the absorption cross-section (Sect. 2.2.4).

2.2. Description of the processes

2.2.1. Optical distance

The spatial distribution of the stars and the dust grains is defined inside a convex model space. The optical distance in a given direction is determined by the dust density distribution $n_d(\boldsymbol{R}_{li})$ at the coordinate $\boldsymbol{R}_{li}$ and the extinction cross-section of transmitted radiation $\tilde{C}_{\rm ext}(\boldsymbol{R}_{li})$

$$\tilde{\tau}_{\rm ext} = \sum_{i=1}^{i_{\rm end}} n_d(\boldsymbol{R}_{li})\tilde{C}_{\rm ext}(\boldsymbol{R}_{li})\Delta l_i\,. \tag{3}$$

The free mean path length

$$l = \sum_{i=1}^{i_{\rm end}} \Delta l_i \tag{4}$$

can be determined from the optical distance $\tilde{\tau}_{\rm ext}$ (see Wolf et al. 1999 for details).

The extinction cross-section is calculated taking into account the state of polarization of the incident radiation (see, e.g., Martin 1974)

$$\tilde{C}_{\rm ext} = \frac{1}{2}(C_{\rm ext}^{\rm TM} + C_{\rm ext}^{\rm TE}) + \frac{1}{2}(C_{\rm ext}^{\rm TM} - C_{\rm ext}^{\rm TE})\cos 2\Psi\frac{Q_0}{I_0} + \frac{1}{2}(C_{\rm ext}^{\rm TM} - C_{\rm ext}^{\rm TE})\sin 2\Psi\frac{U_0}{I_0}\,. \tag{5}$$

Here, Ψ is the angle between the particle frame and the laboratory frame and (I_0, Q_0, U_0, V_0) – the Stokes vector of the incident light. The extinction cross-sections $C_{\rm ext}$ are related to the efficiency factors $Q_{\rm ext}$ by

$$C_{\rm ext} = GQ_{\rm ext}\,, \tag{6}$$

where G is the geometrical cross-section of a spheroid (the area of the particle shadow). This quantity is

$$G(\alpha) = \pi r_{\rm V}^2 \left(\frac{a}{b}\right)^{-2/3} \left[\left(\frac{a}{b}\right)^2 \sin^2\alpha + \cos^2\alpha\right]^{1/2} \qquad (7)$$

for a prolate spheroid and

$$G(\alpha) = \pi r_{\rm V}^2 \left(\frac{a}{b}\right)^{2/3} \left[\left(\frac{a}{b}\right)^{-2} \sin^2\alpha + \cos^2\alpha\right]^{1/2}. \qquad (8)$$

for an oblate spheroid.

In Eq. (5), the superscripts TM and TE are related to two cases of the polarization of incident radiation (TM and TE modes). The efficiency factors $Q_{\rm ext}^{\rm TM,TE}$ are calculated from the solution to the light scattering problem for spheroids obtained by the method of separation of variables (see Voshchinnikov & Farafonov 1993 for details).

2.2.2. Scattering

The solution to the light scattering problem by spheroidal particles is given in a particle reference system related to the rotation axis of a spheroid (in spherical coordinates θ, φ), while the radiative transfer is considered in the laboratory reference system (in spherical coordinates Θ, Φ). We transformed the amplitude matrix from the particle to the laboratory frame and then calculated the scattering matrix using the standard expressions (Bohren & Huffman 1983). In order to check this procedure, the transformation was also done for light scattering by spheroidal particles in the quasistatic approximation where the solution can be written in both coordinate systems (see Voshchinnikov & Farafonov 2000 for details).

The elements of the scattering matrix were normalized using the standard procedure

$$\frac{2}{k^2(C_{\rm sca}^{\rm TM} + C_{\rm sca}^{\rm TE})} \int_0^{2\pi} \int_0^{\pi} F_{11}(\alpha, \Theta, \Phi) \sin\Theta {\rm d}\Theta {\rm d}\Phi = 1, \quad (9)$$

where $C_{\rm sca}$ is the scattering cross-section, $k = 2\pi/\lambda$ the wavenumber and F_{11} the first element of the scattering matrix.

The correctness of computations was checked using the relationships for matrices describing scattering by small particles (see Hovenier & van der Mee 2000 and references therein).

2.2.3. Absorption

The absorption is described by the albedo Λ of the particle which is defined as the ratio of the scattering and extinction cross-sections. It is equal to

$$\Lambda^{\rm TM,TE}(m, r_{\rm V}, a/b, \alpha) = \frac{C_{\rm sca}^{\rm TM,TE}(m, r_{\rm V}, a/b, \alpha)}{C_{\rm ext}^{\rm TM,TE}(m, r_{\rm V}, a/b, \alpha)} \qquad (10)$$

for totally polarized light and

$$\Lambda^{(0)}(m, r_{\rm V}, a/b, \alpha) = \frac{C_{\rm sca}^{\rm TM} + C_{\rm sca}^{\rm TE}}{C_{\rm ext}^{\rm TM} + C_{\rm ext}^{\rm TE}} \qquad (11)$$

for non-polarized light.

While in the case of absorption by spherical particles, the Stokes vector $\hat{I}$ is multiplied by a scalar value, for spheroidal particles the following 4×4 matrix is needed (in the particle frame):

$$\hat{\Lambda}_{\rm part.} = \begin{pmatrix} \tilde{l}_1 & \tilde{l}_2 & 0 & 0 \\ \tilde{l}_2 & \tilde{l}_1 & 0 & 0 \\ 0 & 0 & \tilde{l}_1 & 0 \\ 0 & 0 & 0 & \tilde{l}_1 \end{pmatrix}_{\rm part.} . \qquad (12)$$

Here, $\tilde{l}_1$ and $\tilde{l}_2$ are defined as

$$\tilde{l}_1 = \Lambda^{(0)} = \frac{\Lambda^{\rm TM}}{1 + C_{\rm ext}^{\rm TM}/C_{\rm ext}^{\rm TE}} + \frac{\Lambda^{\rm TE}}{1 + C_{\rm ext}^{\rm TE}/C_{\rm ext}^{\rm TM}},$$
$$\tilde{l}_2 = \frac{\Lambda^{\rm TM}}{1 + C_{\rm ext}^{\rm TM}/C_{\rm ext}^{\rm TE}} - \frac{\Lambda^{\rm TE}}{1 + C_{\rm ext}^{\rm TE}/C_{\rm ext}^{\rm TM}}. \qquad (13)$$

Before applying the albedo matrix, it has to be rotated into the particle frame using the rotation matrix $\hat{R}$

$$\hat{R} = \begin{pmatrix} 1 & 0 & 0 & 0 \\ 0 & \cos 2\Psi & \sin 2\Psi & 0 \\ 0 & -\sin 2\Psi & \cos 2\Psi & 0 \\ 0 & 0 & 0 & 1 \end{pmatrix}. \qquad (14)$$

The absorption process can be described by the expression

$$\hat{I}_{\rm after} = \hat{R}^{-1}\, \hat{\Lambda}_{\rm part.}\, \hat{R}\, \hat{I}_{\rm before}\, . \qquad (15)$$

2.2.4. Re-emission

The radiation emitted by a spheroidal particle in the particle frame can be written as:

$$\begin{pmatrix} I_0 \\ Q_0 \\ U_0 \\ V_0 \end{pmatrix}_{\rm part.} = \begin{pmatrix} (C_{\rm abs}^{\rm TM} + C_{\rm abs}^{\rm TE})/2 \\ -(C_{\rm abs}^{\rm TM} - C_{\rm abs}^{\rm TE})/2 \\ 0 \\ 0 \end{pmatrix}_{\rm part.} , \qquad (16)$$

where $C_{\rm abs}$ is the absorption cross-section.

3. Numerical aspects

3.1. Discretization of the scattering distribution function

The calculation of the elements of the scattering matrix $\hat{F}(m, r_{\rm V}, a/b, \alpha, \Theta, \Phi)$ and efficiency factors $Q_{\rm sca,ext}^{\rm TM,TE}(m, r_{\rm V}, a/b, \alpha)$ for a single particle with fixed equivolume radius r_V, aspect ratio a/b, and refractive index m requires several minutes of computer time. These quantities were precalculated before starting the radiative transfer modelling. The precalculated and therefore discretely distributed values have to answer two contradicting demands:

1. The main features (local minima/maxima) of the scattering matrix elements (and/or derived quantities, for instance, the polarization of singly scattered light) must be included in the discrete distributions as a function of α, Θ, and Φ (see Figs. 1 and 2).

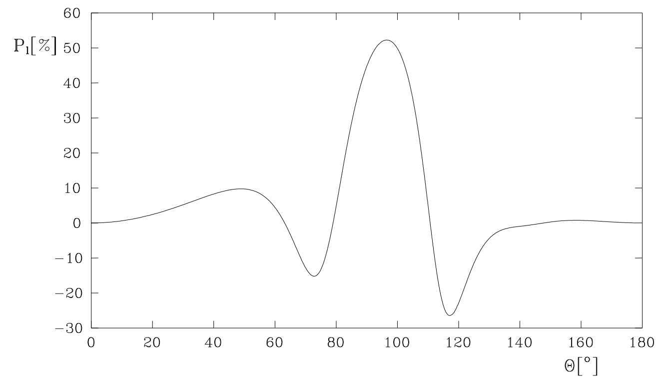

Fig. 1. The linear polarization of radiation $P_l(\Theta)$ after the first scattering by a prolate spheroidal particle with refractive index $m = 1.7 + 0.03i$, equivolume radius $r_V = 0.20\,\mu$m, aspect ratio $a/b = 4$ and the incidence angle $\alpha = 0°$. The wavelength of incident radiation is $\lambda = 0.628\,\mu$m. To avoid skipping of local minima/maxima a step size smaller than 5° for Θ is required (see Sect. 3.1).

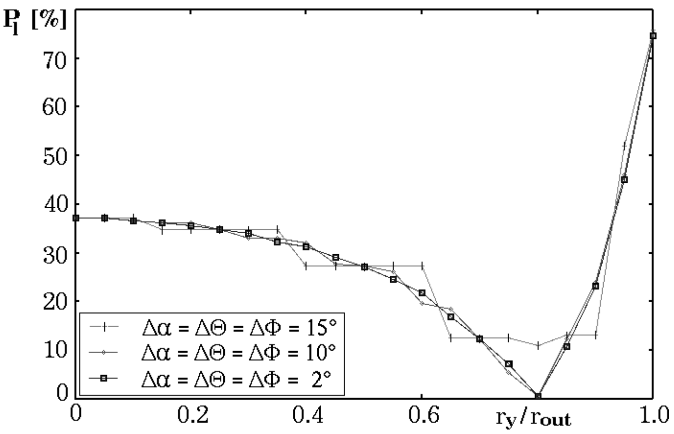

Fig. 2. The degree of linear polarization in the midplane of the polarization map shown in Fig. 4[A] in dependence of the projected distance. Grain parameters are described in Sect. 4.1. Three different discretizations for the angles α, Θ, and Φ were applied ($\Delta\alpha = \Delta\Theta = \Delta\Phi = 2°, 10°$, and 15°). Only the smallest step gives a sufficient approximation to the analytical solution presented in Fig. 4 [B1] (see Sect. 3.1 and 4.2 for discussion).

2. The required computer memory to store the precalculated values which is inversely proportional to the chosen values of $\Delta\alpha$, $\Delta\Theta$, and $\Delta\Phi$ has not to exceed the computer capacities.

While the first demand requires very small steps, the second one calls for the opposite. In our simulations we use $\Delta\alpha = \Delta\Theta = \Delta\Phi = 2°$.

3.2. Radiative transfer aspects

3.2.1. Scattering

The scattered photon flight direction is randomly chosen from the discrete distribution of the normalized phase function. The probability of a photon to be scattered into the direction (Θ, Φ) is proportional to the value of the first element of the scattering matrix $F_{11}(\alpha, \Theta, \Phi)$.

3.2.2. Test photon transfer

The extinction cross section $\tilde{C}_{\rm ext}$ (see Eq. (5)) has to be determined for every step of a photon flight between two scatterings. In the case of the RT in a medium with aligned non-spherical grains, the value of the step of the photon free path is determined not only by the scale of the density structure (as for spherical particles) but also by the degree of spatial variations of the grain alignment. Owing to this and more complex treatment of the scattering process compared with spherical grains, the total simulation runtime is by an order of magnitude larger for spheroids than for spheres.

4. Test simulations

4.1. General remarks

The best way to test any radiative transfer code would be the comparison of the results with those obtained with another technique. Because this code is the *first* that provides the treatment of multiple scattering of polarized light by aligned non-spherical particles, a lack of suitable test cases for comparison is evident. Nevertheless, in the following we present test calculations which confirm the correct implementation of the new scattering mechanism into the RT code.

For test simulations we used the particles with following parameters:
oblate spheroids,
refractive index $m = 1.7 + 0.03i$,
equivolume radius $r_V = 0.1\,\mu$m,
aspect ratio $a/b = 2.0$,
wavelength of incident radiation $\lambda = 0.628\,\mu$m.
Then the grain size parameter is $x_V = 2\pi r_V/\lambda = 1$. The picket fence (static) orientation of the particles rotation axes parallel to the z-axis was assumed in all cases.

4.2. Single scattering

4.2.1. Linear polarization

Firstly, we consider the single scattering in a thin layer at the surface of an hemisphere (see Fig. 3). The ratio of the inner radius of the shell to the outer one $r_{\rm in}/r_{\rm out}$ amounts to 0.99.

We compare the resulting polarization map with that obtained by Matsumura & Seki (1996).[1] In Fig. 4 the comparison of the polarization degree as a function of the projected distance from the centre along three different lines in the polarization map is shown. These graphs as well as the polarization pattern (see for comparison Fig. 2 from Matsumura & Seki 1996) are in perfect agreement.

[1] The numerical data in tabular form were given by Matsumura (1999).

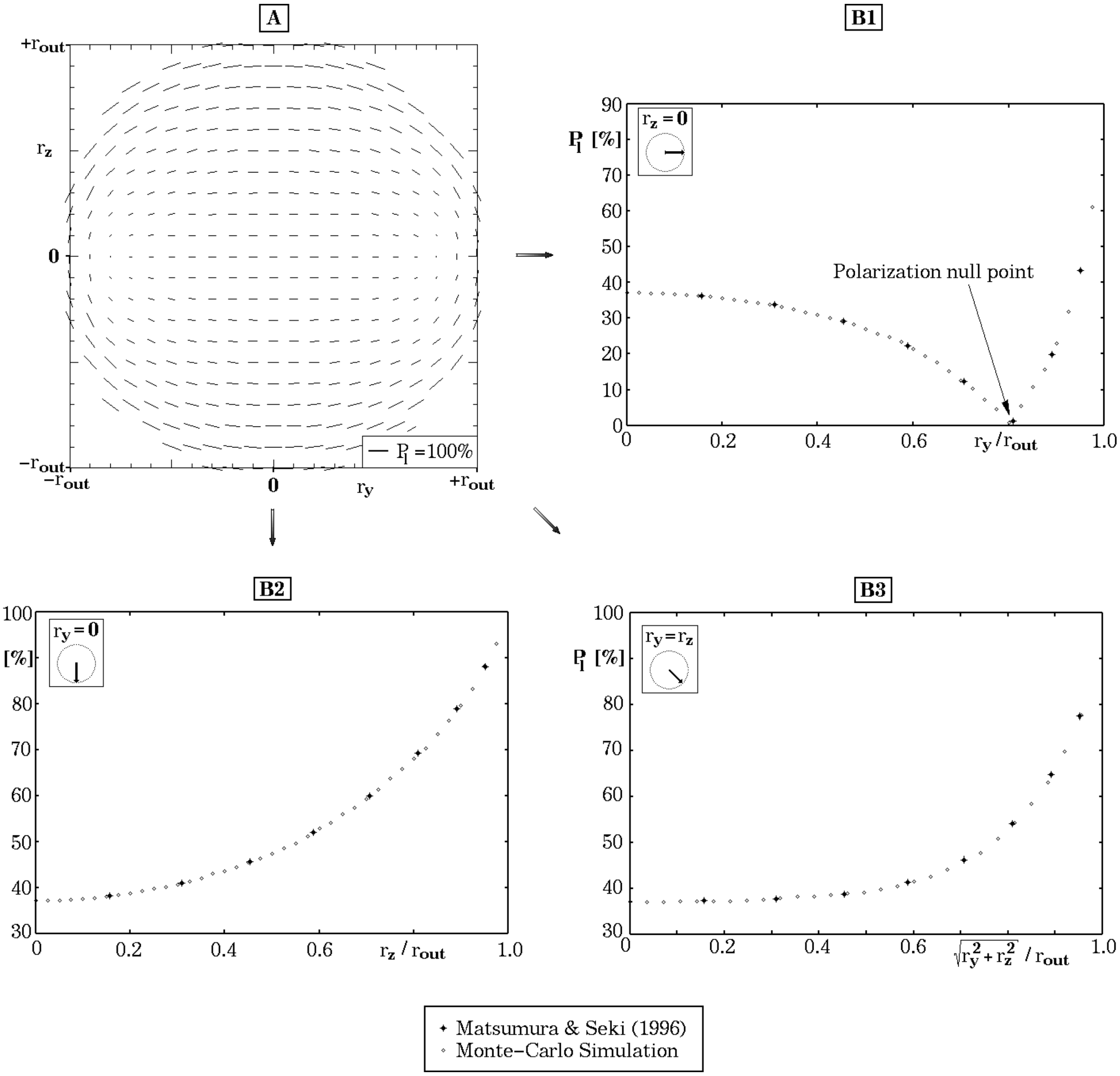

Fig. 4. The results of test calculations for the comparison with the data of Matsumura & Seki (1996). Grain parameters are described in Sect. 4.1. [A]: Polarization map of the configuration shown in Fig. 3. Only singly scattered radiation is considered. [B1]...[B3]: The degree of linear polarization as a function of the projected distance from the centre along three different directions. The projected distance $r/r_{\rm out}$ is connected with the scattering angle as $r/r_{\rm out} = \arcsin\Theta$. [B1]: $P_{\rm l}$ in the midplane of polarization map; [B2]: $P_{\rm l}$ perpendicular to the midplane; [B3]: $P_{\rm l}$ along a line being inclined by 45° to the midplane.

In contrast to polarization maps obtained for model configurations with the same geometry, but containing spherical dust grains, the polarization pattern is *not* centro-symmetric. This is because of the azimuthal asymmetry of light scattering by aligned non-spherical particles. The net polarization in this case is not equal to zero.

Qualitatively, the polarization pattern is quite similar to that of an young stellar object surrounded by a spherical shell and an optically thick disk seen edge-on (parallel polarization pattern is due to light scattering on the disk surface; centro-symmetric polarization pattern is due to light scattering in the circumstellar environment). The corresponding RT simulations with spherical dust grains have been performed earlier (see, e.g., Ménard 1988; Fischer 1994). The most interesting feature of the pattern is the presence of polarization null points (see Figs. 4[A] and 4[B1]). They have been observed in a number of objects (e.g., Scarrott et al. 1989; Hajjar & Bastien 1996; Kastner & Weintraub 1996). These null points are usually interpreted as the indicators for the "outer edge" of a circumstellar disk (transition from the optically thick disk to the optically thin shell). Although this explanation is very plausible, the simulations presented here show that

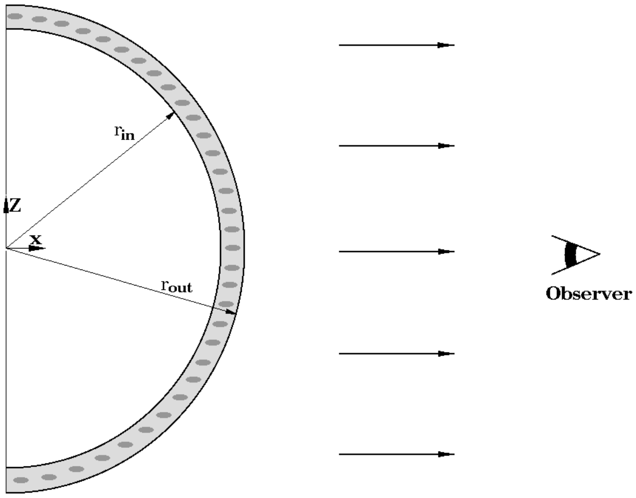

Fig. 3. Model configuration for comparison with the results of Matsumura & Seki (1996). It consists of a thin dust layer at the surface of a hemisphere. The ratio of the inner radius to the outer one amounts to $r_{\rm in}/r_{\rm out} = 0.99$. The shell contains oblate grains, whereby their rotation axes (b) are oriented parallel to the z-axis. The dark grey oval pattern symbolizes the aligned grains. The configuration is shown for $y = 0$ (xz-plane, the azimuthal angle $\Phi = 180°$). An observer sees the radiation at the scattering angles $\Theta = 0° - 90°$. In this case the condition $\Theta + \alpha = 90°$ is satisfied in all points of dust layer.

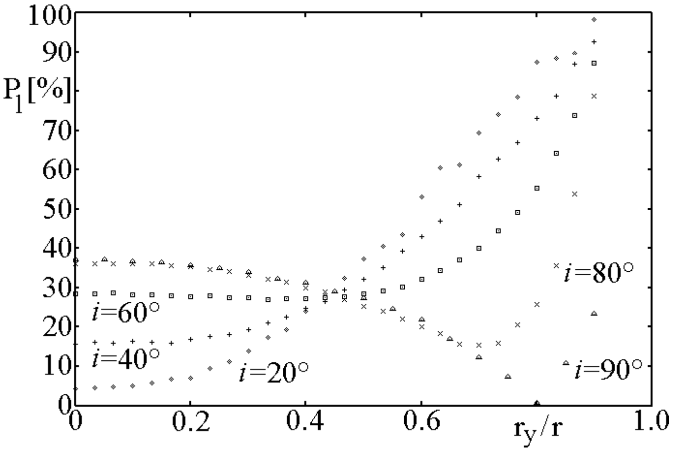

Fig. 5. The degree of linear polarization in dependence of the projected distance for tilted dust configurations.

uniformly aligned grains (possibly by external magnetic field) may produce a similar polarization pattern.

The "polarization null points" appear and in the case of prolate particles with the same parameters $[m, r_{\rm V}, a/b]$ arranged similar to oblate particles in Fig. 3 (i.e., their small axes are parallel to the z-axis). The polarization null points can then be seen below and above the center of the polarization map, when the degree of linear polarization is plotted as a function of the projected distance $r_z/r_{\rm out}$ (see also Fig. 12).

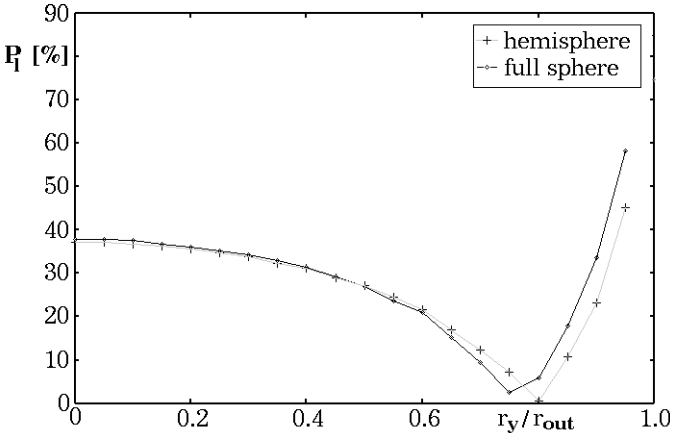

Fig. 6. The degree of linear polarization in dependence of the projected distance. Influence of the backward scattering is illustrated.

4.2.2. Tilted dust configurations

While the polarization pattern in Fig. 4 is shown only from a position perpendicular to the z-axis ($i = 90°$), Fig. 5 demonstrates the behaviour of the degree of linear polarization in the midplane of the polarization map appeared at different inclinations of the z-axis to the line of sight. It turns out that the local polarization minimum (the "polarization null point" or the reversal of polarization in the case $i = 90°$) are present at large inclination angles i only.

It is important to note, that the polarization pattern (and therefore also the net polarization degree) for aligned non-spherical particles depends on the viewing angle even in the case of a one-dimensional density distribution. In contrast to this, no dependence of the polarization on the inclination exists for spherical particles.

4.2.3. Influence of the backward scattering

As a first step away from the very artificial configuration described above, we consider the radiative transfer in a thin spherical shell instead of the hemisphere shown in Fig. 3. Then, backward scattering in the hemisphere opposite to the observers position where $\Theta = 90° + \alpha$ has to be taken into account. The results are shown in Fig. 6. The addition of backscattered radiation shifts the position of minimum of the linear polarization to a smaller projected radius.

4.2.4. Circular polarization

In Fig. 7 the circular polarization is plotted for the model configuration discussed in this Section. This map is the counterpart to the map of linear polarization shown in Fig. 4[A]. The circular polarization is equal to zero in the midplane and along the line through the center perpendicular to the midplane. The net circular polarization from the configuration is also equal to zero. A counterpart of the linear polarization null points in the midplane could not be found. The maximum values are observed at the

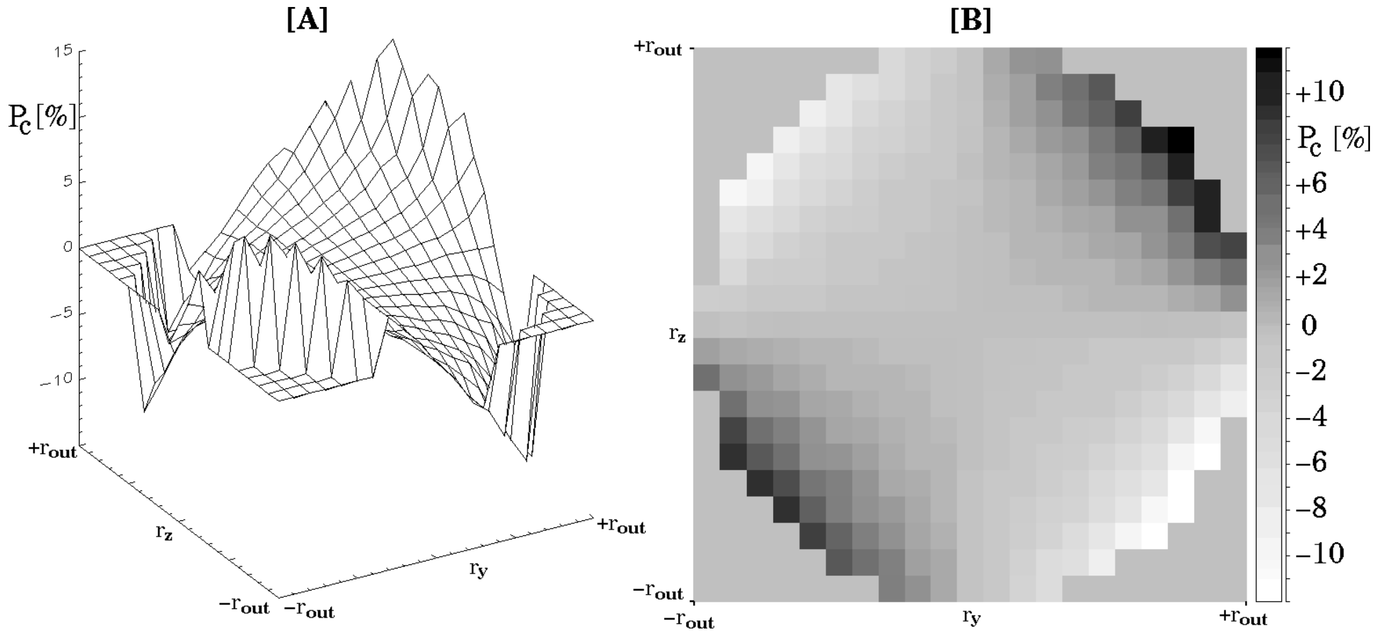

Fig. 7. The circular polarization of the scattered radiation arising from the configuration shown in Fig. 3. Grain parameters are described in Sect. 4.1. Deviations from the total symmetry result from the statistical noise of the Monte Carlo simulation.

ends of lines inclined to the z-axis by $\pm 45°$. These points correspond to the light scattering by particles with values of $\alpha = 45°$, $\Theta = 90°$ and $\Phi = 90°$ $(270°)$.

4.3. Multiple scattering

To test the radiative transfer with multiple scattering, we consider model configurations for which the dust density distribution, the dust grain orientation, and the irradiation characteristic are centro-symmetric with respect to the observer's position. The resulting polarization pattern is therefore also centro-symmetric: the polarization vectors are oriented perpendicular or parallel to the configuration radius vector in dependence on the refractive index and the grain size parameter $x_{\rm V}$. The integral (net) linear and circular polarization has to be zero. Because this property of centro-symmetric configurations does not depend on its optical thickness, it can be used as a test of the single and multiple scattering case.

We considered the following dust configurations containing either oblate or prolate grains:

1. – spherical dust shell with a point-like radiation source in the centre;
   – particle rotation axes either parallel or perpendicular to the radius vector;
2. – cylindrical dust shell with a point-like radiation source on its rotation axis;
   – particle rotation axes either parallel or perpendicular to the radius vector which is oriented perpendicular to the rotation axis of the cylinder.

While for the first configuration the net polarization is equal to zero for every position of the observer, for the second configuration this is the case only if the observer's line of sight is oriented perpendicular to one of the two cylinders footprints. In all cases we arrived to the expected results.

5. Results and discussion

5.1. General remarks

If we consider the radiative transfer in a medium consisting of spherical dust grains, scattering is the only mechanism to produce or modify the polarization of the incident radiation. In the case of aligned spheroidal grains, the processes of photon absorption and re-emission may also fabricate or change polarization. Because of the obvious complexity of the problem, we decided to separate the investigation of the influence of these three mechanisms on polarization. The aim of the simulations discussed below was to outline the basic features of polarization arising from the *light scattering* by spheroidal grains. The additional influence of absorption and re-emission will be discussed in future publications.

For this reason the following approximations are introduced:

1. The grain albedo is assumed to be that of spherical grains with the equivolume radius $r_{\rm V}$ and is therefore a scalar. Then, the absorption process decreases the intensity of the incident radiation but does not modify the state of polarization.
2. We do not consider thermal dust re-emission.

Our standard model configuration consists of a spherical shell with a point-like, isotropic radiation source in its centre. The ratio of the inner radius of the shell to the outer one is assumed equal to $r_{\rm in}/r_{\rm out} = 0.5$. Its variations are discussed in Sect. 5.2. We consider the single

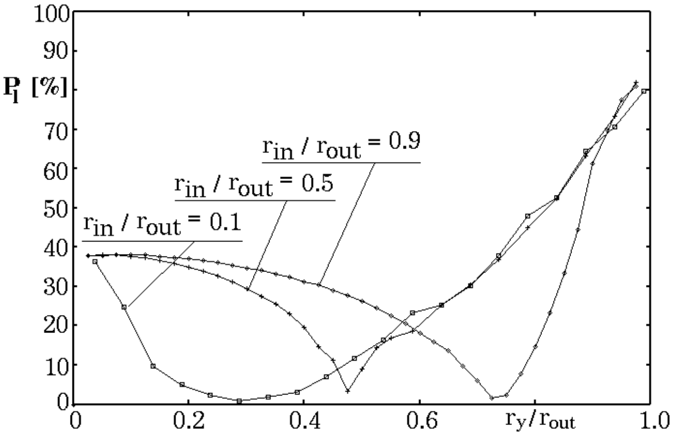

Fig. 8. The degree of linear polarization in dependence of the projected distance. The effect of the transition from a geometrically thin to a geometrically thick spherical shell is illustrated. Oblate particles, other grain and shell parameters are described in Sect. 5.1.

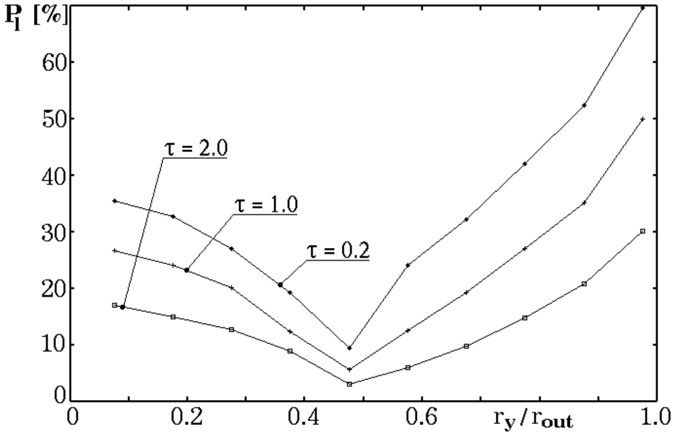

Fig. 9. The degree of linear polarization in dependence of the projected distance. The effect of the transition from an optically thin to an optically thick spherical shell is illustrated. Oblate particles, other grain and shell parameters are described in Sect. 5.1.

size ($r_V = 0.10\,\mu$m) prolate or oblate spheroidal particles of the same shape ($a/b = 2$) with the refractive index $m = 1.7 + 0.03i$. The particles are distributed in the shell with the density profile $n(r)$

$$n(r) \propto r^{-1}\,. \tag{17}$$

The variations of the grain parameters are considered in Sect. 5.3. The non-rotating particles are totally aligned with rotation axes parallel to the z-axis located in the sky plane (the picket fence orientation, $i = 90°$). The optical thickness of the shell at the wavelength of the simulated radiative transfer ($\lambda = 0.628\,\mu$m) is 0.2 along the z-axis, i.e. $\tau_z(0.628\,\mu\mathrm{m}) = 0.2$.[2] Because of the chosen grain alignment, τ_z is proportional to the extinction cross section in the case of light incident parallel to the grain rotation axis, $\tau_0 = \tau_z \propto C_{\mathrm{ext}}(0°)$. In other directions, the optical thickness of the shell may be found as $\tau_\alpha = \tau_z C_{\mathrm{ext}}(\alpha)/C_{\mathrm{ext}}(0°)$ and, in particular, along the line of sight (x-axis) and the y-axis we have $\tau_x = \tau_y = \tau_{90°} = \tau_z C_{\mathrm{ext}}(90°)/C_{\mathrm{ext}}(0°)$. Using Eq. 5 for non-polarized stellar radiation and the standard model described above, we have $\tau_{90°} \approx 0.35$ (prolate grains) and $\tau_{90°} \approx 0.13$ (oblate grains), if $\tau_0(0.628\,\mu\mathrm{m}) = 0.2$. For more elongated or flattened particles ($a/b = 10$), these values become equal to $\tau_{90°} \approx 0.68$ and 0.082 for prolate and oblate grains, respectively.

5.2. Dependence on shell parameters

The polarization pattern strongly depends on the inner radius of the spherical shell. This is demonstrated in Fig. 8, where the degree of linear polarization in the midplane is shown for three ratios of the inner to the outer radius of the shell.

[2] The effects of variations of the optical thickness are discussed in Sect. 5.2.

Decreasing the ratio, the characteristic polarization null points shift towards the star. It has to be noted, that generally the polarization null point is not located at the position of the projected inner radius ($r_{\mathrm{in}}/r_{\mathrm{out}} \neq r_{\mathrm{y}}/r_{\mathrm{out}}$). The location, relative depth and width of the area where the polarization changes the sign depends on the geometrical thickness of the shell and grain parameters (see Sect. 5.3). The density profile used leads to a preferred photon scattering near a narrow region at the inner boundary of the shell. The shift of the polarization null point is therefore mainly caused by the change of the inner radius r_{in}. For the explanation of the broadening in the case $r_{\mathrm{in}}/r_{\mathrm{out}}$=0.1, the scattering events in regions where $r \gg r_{\mathrm{in}}$ must be taken into account. Thus, the observed structure results from the superposition of the light scattering in the regions with a low level of polarization.

In the case of small optical thickness, the main contribution to the resulting polarization is from first one-two scatterings (Voshchinnikov & Karjukin 1994; Voshchinnikov et al. 1995). As one can see from Fig. 9, the polarization $P_{\mathrm{l}}(r_y/r_{\mathrm{out}})$ in the midplane decreases with increasing optical thickness. The same behaviour was found for the polarization perpendicular to the midplane $P_{\mathrm{l}}(r_z/r_{\mathrm{out}})$. In general, the position of the local polarization minimum is not strongly influenced by the optical thickness.

Integrating the images for the Stokes parameters I, Q, U, we estimate the summary linear polarization from our spherical dust configuration as one observes from the position perpendicular to the z-axis. Because of the symmetry, it is the same along the x and y-axes

$$P_{\mathrm{l},\,90°} = \frac{F^{\mathrm{p}}_{\mathrm{sca},\,90°}}{F_\star \exp\left[-\tau^{\mathrm{ext}}_{90°}\right] + F_{\mathrm{sca},\,90°}}\,, \tag{18}$$

where $F_{\mathrm{sca},\,90°}$ and $F^{\mathrm{p}}_{\mathrm{sca},\,90°}$ are the scattered and polarized scattered radiation from the configuration.

Table 1. The maximum linear polarization from the spherical shell containing perfectly aligned spheroidal grains

a/b	Oblate particles	Prolate particles
1.1	3.6 %	3.0 %
2	25	20
4	43	31
10	57	41

For the models presented in Fig. 9, the resulting polarization is P_l = 4%, 9%, and 8%, if $\tau = 0.2$, 1 and 2, correspondingly.

Excluding the stellar radiation (first term in the denominator in Eq. (18)), we can find the maximum degree of the observed linear polarization

$$P_{l,90^\circ,\max} = \frac{F^{p}_{\mathrm{sca},90^\circ}}{F_{\mathrm{sca},90^\circ}}. \tag{19}$$

It is equal to $P_{l,90^\circ,\max} = 23\pm1\,\%$, $15\pm1\,\%$, and $9.1\pm1\,\%$, if $\tau = 0.2$, 1 and 2, correspondingly.

5.3. Dependence on dust grain parameters

Figure 10 shows the midplane polarization $P_l(r_y/r_{\mathrm{out}})$ for oblate and prolate grains of three equivolume radii. The behaviour of polarization for particles with $r_V = 0.05\,\mu$m and $0.1\,\mu$m is rather similar, while the polarization produced by the largest particles ($r_V = 0.2\,\mu$m) is the smallest and is almost independent of the projected radius. This feature reflects the fact of decreasing polarizing efficiency of large particles (Voshchinnikov & Farafonov 1993). Because the manner of polarization for prolate grains in the direction perpendicular to the midplane is similar to that for oblate grains in the midplane and vice versa (see also Fig. 12), the resulting polarization for particles of both types is quite similar. The maximum polarization — excluding the direct, non-scattered stellar radiation — amounts to $P_{l,90^\circ,\max} = 20\,\%$ (16 %), 25 % (20 %) and 11 % (10 %) for oblate (prolate) grains with equivolume radii $r_V = 0.05\,\mu$m, $0.1\,\mu$m and $0.2\,\mu$m, respectively.

The distribution of the linear polarization $P_l(r_y/r_{\mathrm{out}})$ in the midplane of spherical shell is plotted in Fig. 11 for particles with four aspect ratios a/b. The polarization minima in the midplane ($r_z = 0$) appear for oblate grains only. Their position shifts to outer projected radii r_y/r_{out} with increasing aspect ratio. If $a/b \to 1$, the location of the polarization null point leads to $r_y/r_{\mathrm{out}} \to 0$. This is consistent with the behaviour of the degree of linear polarization for spherical grains where the null polarization can be found at the centre for the scattering angle $\Theta = 0^\circ$. The resulting polarization for oblate and prolate grains of different shape are given in Table 1. Note that the polarization produced by oblate particles is larger in all cases.

An additional effect is seen from the intensity maps. In Fig. 12, the images with overlaid polarization pattern corresponding to the intensity and linear polarization of scattered light are shown for oblate and prolate grains with the aspect ratios a/b=1.1 and 2. In the case of nearly spherical grains ($a/b = 1.1$), the ring-like structure is clearly seen for oblate as well as for prolate grains. Otherwise, in the case of $a/b = 2$ the intensity maxima appear at the points of intersection with the $z(y)$-axis for oblate (prolate) grains. In both cases, the corresponding axis is parallel to the minor (b) axis of grains. Increasing the aspect ratio a/b, this effect is strengthened. Note that the net polarization from the spherical configuration considered arises in the inner parts of the shell because the polarization pattern from the outer regions is centro-symmetric and the polarization would be cancelled. The direction of the resulting polarization is parallel to the major (a) axis of grains that is similar to the case of dichroic polarization.

6. Conclusions

We presented the first solution to the radiative transfer problem in dust configurations containing aligned non-spheroidal dust grains. Our main aim was to discuss the effects of light scattering by spheroidal dust grains in simple (spherical) dust configuration containing perfectly aligned particles.

The most remarkable features of the simulated linear polarization maps are the polarization null points where the reversal of polarization occurs. They appear in the case when the grain alignment axis is perpendicular to the line of sight. Symmetrically to the polarization null points there are the maxima on the intensity maps.

In contrast to spherical grains, single scattering by spheroidal grains may cause circular polarization. The maps of circular polarization has the sector-like structure with maxima at the ends of line inclined to the grain alignment axis by $\pm 45^\circ$.

The next steps of the started investigation will include the consideration of light scattering by the partly aligned rotating particles and the polarized re-emission of grains in different dust configurations. This will immediately lead to an improved interpretation and therefore better understanding of far-infrared polarization maps (e.g., of polarization maps of Bok globules) where re-emission by aligned non-spherical dust grains is the main polarization mechanism. So, it would be provided a basis for investigations of the structure of the magnetic fields in these objects which are in the most cases assumed to cause grain alignment.

Acknowledgements. We appreciate the discussions of light scattering by non-spherical particles with Viktor Farafonov and Bernhard Michel. We wish to thank M. Matsumura for providing his results for comparison. This research was supported by the DFG grant Ste 605/10 within the program "Physics of star formation" and by grants of the Volkswagen Foundation and INTAS (Open Call 99/652).

References

Bastien, P., & Ménard, F., 1988, ApJ 326, 334

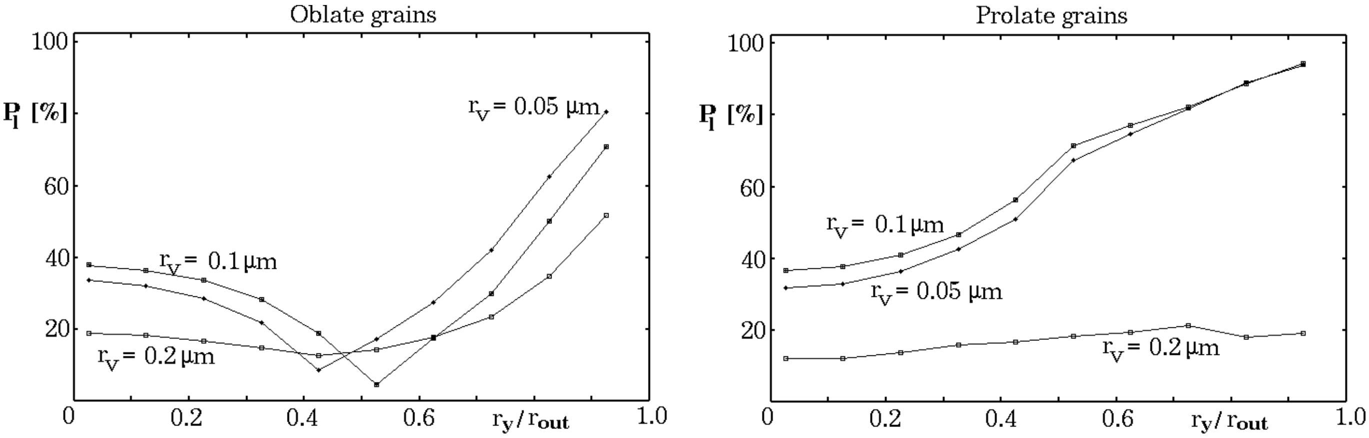

Fig. 10. The degree of linear polarization in dependence of the projected distance. The effect of the variations of the equivolume radius r_V is illustrated.

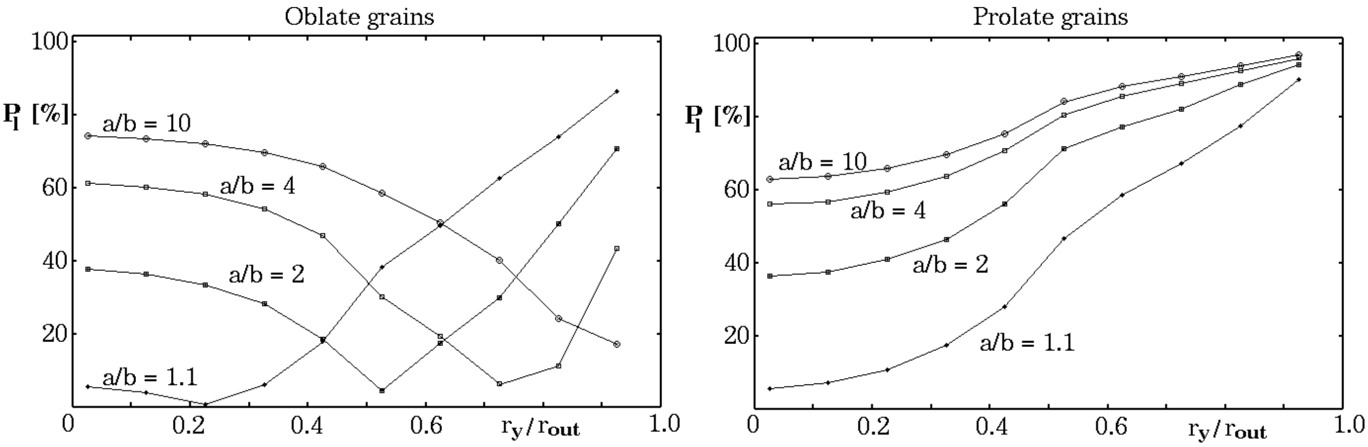

Fig. 11. The degree of linear polarization in dependence of the projected distance. The effect of the variations of the grain shape (the aspect ratio) is illustrated.

Bohren, C.F., & Huffman, D.R., 1983, Absorption and scattering of light by small particles. John Wiley & Sons, New York

Chrysostomou, A., Gledhill, T., Ménard, F., et. al., 2000, MNRAS, 312, 103

Daniel, J.-Y., 1980, A&A 87, 204

Dollfus, A., & Suchail, J.-L., 1987, A&A 187, 669

Elvius, A., & Hall, J.S., 1967, Lowell Obs. Bull. 7, 17

Fischer, O., 1994, PhD Thesis, Friedrich-Schiller-Universität, Jena

Fischer, O., Henning, Th., Yorke, H.W., 1994, A&A 284, 187

Gledhill, T., & McCall, A., 2000, MNRAS 314, 123

Hajjar, R., & Bastien, P., 1996, in ASP Conf. Ser. 97, Polarimetry of the Interstellar Medium, eds. W.G. Roberge, & D.C.B. Whittet, 355

Hovenier, J.W., & van der Mee, V.M., 2000, in Light Scattering by Nonspherical Particles, eds. M.I. Mishchenko et al., (Academic Press, San Francisco), 61

Il'in, V.B., & Henning, Th., 2000, A&A, submitted

Johnson, J.J., & Jones, T.J., 1991, AJ 101, 1735

Kastner, J.H., & Weintraub, D.A., 1996, in ASP Conf. Ser. 97, Polarimetry of the Interstellar Medium, eds. W.G. Roberge, & D.C.B. Whittet, 212

Kim, S.H., & Martin, P.G., 1995, ApJ 444, 293

Martin, P.G., 1974, ApJ 187, 461

Matsumura, M., & Seki, M., 1996, in ASP Conf. Ser. 97, Polarimetry of the Interstellar Medium, eds. W.G. Roberge, & D.C.B. Whittet, 63

Matsumura, M., 1999, private communication

Ménard, F., 1988, PhD Thesis, Université de Montréal

Onaka, T., 2000, ApJ 533, 298

Scarrott, S., Draper, P.W., Warren Smith, R.F., 1989, MNRAS 237, 621

Voshchinnikov, N.V., 1990, SvA 34, 535

Voshchinnikov, N.V., 1998, IAU Symp. 191, p. 3-16

Voshchinnikov, N.V., & Farafonov, V.G., 1993, Ap&SS 204, 19

Voshchinnikov, N.V., & Farafonov, V.G., 2000, in preparation

Voshchinnikov, N.V., & Karjukin, V.V., 1994, A&A 288, 883

Voshchinnikov, N.V., Grinin, V.P., Karjukin, V.V., 1995, A&A 294, 554

Wolf S., Fischer O., Pfau, W., 1998, A&A 340, 103

Wolf, S., & Henning, Th., 2000, Computer Physics Comm., 132, 166

Wolf, S., Henning, Th., Stecklum, B., 1999, A&A 349, 839

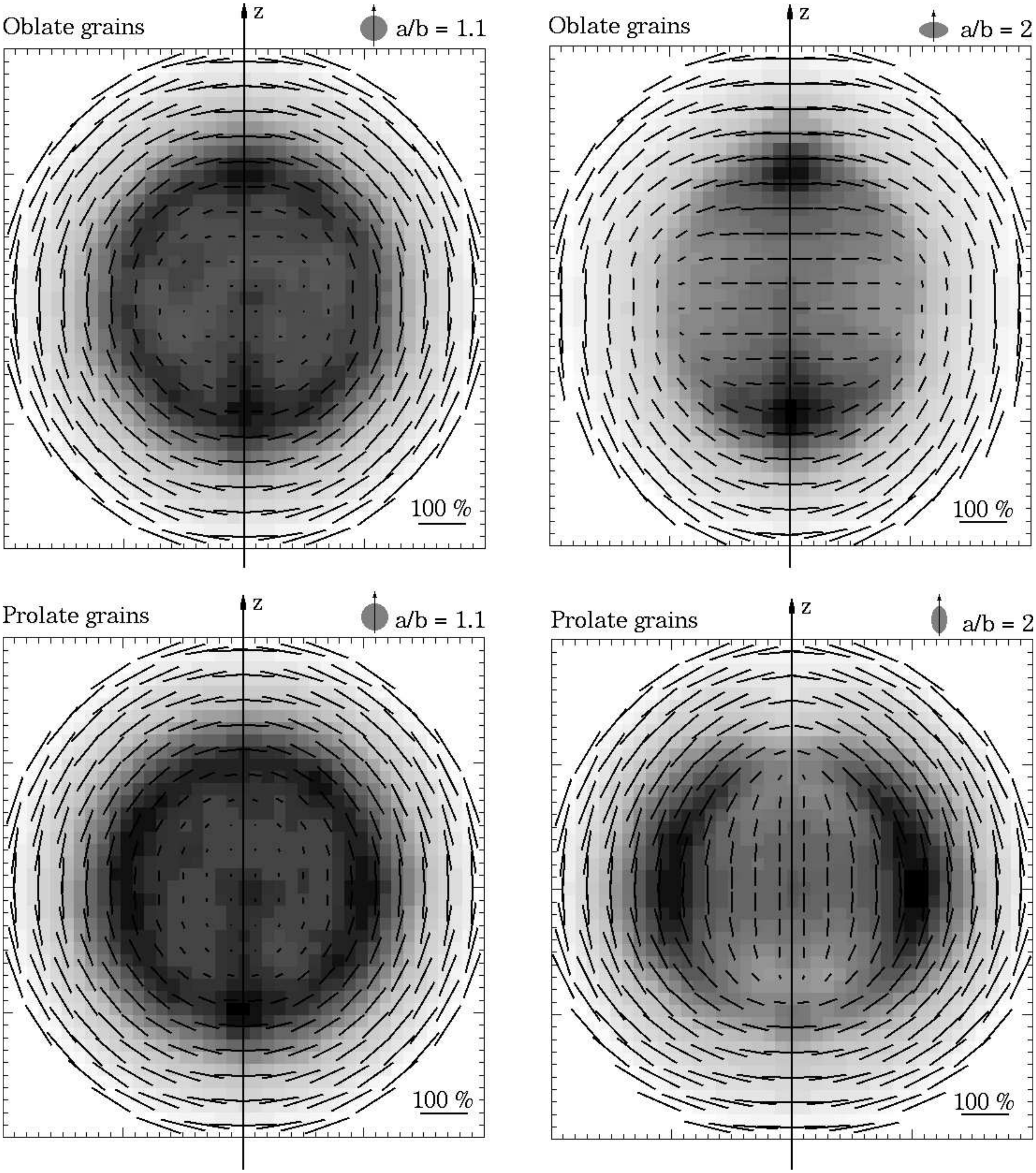

Fig. 12. Images with overlaid polarization pattern corresponding to the intensity and linear polarization of scattered light. Darker regions symbolize brighter areas. Because of chosen shell and grain parameters (see Sect. 5.1) the brightest knots appear at the inner boundary of the shell.